MSDE IChemE ADVANCING CHEMICAL ENGINEERING WORLDWIDE

Semi-Quantitative Design of Black Phosphorous Field-Effect Transistor Sensors for Heavy Metal Ion Detection in Aqueous Media

SCHOLARONE™ Manuscripts

Design, System, Application Statement

Heavy metal ion pollution has become a pressing problem worldwide. Field-effect transistor (FET) sensors are one of the most promising technologies for real-time, ultrasensitive detection of heavy metal ions. We have semi-quantitatively simulated the sensing performance of 2D nanomaterial-based FET sensors and designed experiments using a black phosphorus (BP) nanosheet-based sensor platform to validate sensing mechanisms (charge transfer vs. electrostatic gating). The two distinctive sensing mechanisms can be engineered to synergistically enhance the sensor performance (e.g., higher sensitivity and broadened dynamic response range). Therefore, our model provides guidelines for quantitative molecular design of future FET sensors and sensor systems with optimized performance. Furthermore, the generic model is applicable to other 2D nanomaterial-based FET devices useful for a wide range of applications.

Journal Name

ARTICLE

Semi-Quantitative Design of Black Phosphorous Field-Effect Transistor Sensors for Heavy Metal Ion Detection in Aqueous Media

Jingbo Chang[a†], Haihui Pu[a†], Spencer A. Wells[b], Keying Shi[d], Xiaoru Guo[a], Guihua Zhou[a], Xiaoyu Sui[a], Ren Ren[a], Shun Mao[a,e], Yantao Chen[a], Mark C. Hersam[b,c], Junhong Chen[a*]

Two-dimensional (2D) crystalline nanomaterial based field-effect transistor (FET) water sensors are attracting increased attention due to their low cost, portability, rapid response, and high sensitivity to aqueous contaminants. However, a generic model is lacking to aid the sensor design by describing direct interactions between metal ions and 2D nanomaterials. Here, we report a broadly applicable statistical thermodynamics model that describes the behavior of FET sensors (e.g., lower detection limit) by relying only on the ion concentration and intrinsic properties of the sensor material such as band gap and carrier effective mass. Two regimes of sensing mechanism (charge transfer vs. electrostatic gating) were predicted, depending on the relative size of the Debye screening length in the sensor material and the distance between adsorbed ions. At a lower ion adsorption density, the charge transfer effect is dominant, while the evolution from charge transfer into electrostatic gating effect occurs at a higher adsorption density as the distance between adsorbed ions approaches the Debye length. Owing to its tunable band gap, black phosphorus (BP) nanosheet FET sensors were selected to semi-quantitatively validate the model including the predicted evolution between the two sensing regimes. Among Na^+, Mg^{2+}, Zn^{2+}, Cd^{2+}, Pb^{2+}, and Hg^{2+} ions, BP nanosheet FET sensors were more responsive to Hg^{2+} ions for probe-free detection. The theoretical lower detection limit of Hg^{2+} ions can reach 0.1 nM (0.1 fM) in tap (deionized) water.

Introduction

Heavy metal ion pollution has been an ongoing problem worldwide for many decades.[1-4] Heavy metal ions are poisonous and may cause serious damage to human organs, tissues, bones, and nervous system. For example, mercury[5-7] can be inhaled or absorbed through the skin, damaging the nervous system; impairing hearing, speech, vision, gait, and involuntary muscle movements; and corroding skin and mucous membranes.[8-10] To minimize the risks of toxic metals to human health and the environment,[11-14] it is imperative to develop real-time sensors for monitoring heavy metal ion contamination in water, especially tap water.[15] To this end, an *in situ* sensing platform is desirable to quickly enact safety measures before harmful contamination levels are reached.[16-20] To date, various techniques based on spectroscopic,[21, 22] electrochemical,[23-25] and electrical conductance measurements[26] have been developed to detect heavy metal ions. Among these, field-effect transistor (FET) sensors are particularly attractive due to their convenient fabrication, portability, low-cost, real-time response, selectivity, and ultrahigh sensitivity.[27, 28]

A typical FET sensor consists of a channel material, source/drain electrodes, and gate oxide, and senses the presence of target metal ions through conductance changes in the channel material upon metal ion adsorption. Presently, two-dimensional (2D) nanomaterials, e.g., graphene, transition metal dichalcogenides and black phosphorous (BP),[29-33] are top channel material candidates for FET sensor applications. This potential is due to the high surface-to-volume ratio of 2D nanomaterials, implying a high surface adsorption capacity of target analytes,[34] while the thickness/strain-dependent electronic properties of 2D-layered nanomaterials allow for the adjustment of sensor characteristics through manipulating layer number/strain.[35, 36] Previous studies on 2D nanomaterial FET water sensors have relied on semiconductors based on thermally reduced graphene oxide (rGO)[37, 38] and MoS_2.[39] These sensors require surface-coated nanoparticles decorated with specific probes to enhance metal ion adsorption and selectivity; e.g., thioglycolic acid functionalized Au nanoparticles were used to detect mercury ions.[37]

[a.] Department of Mechanical Engineering, University of Wisconsin-Milwaukee, 3200 North Cramer Street, Milwaukee, Wisconsin, 53211, USA

[b.] Department of Materials Science and Engineering, Northwestern University, Evanston, Illinois, 60208, USA

[c.] Department of Chemistry, Northwestern University, Evanston, Illinois, 60208, USA

[d.] Key Laboratory of Functional Inorganic Material Chemistry, Ministry of Education of the People's Republic of China, Heilongjiang University, Harbin 150080, P. R. China

[e.] State Key Laboratory of Pollution Control and Resource Reuse, School of Environmental Science and Engineering, Tongji University, 1239 Siping Road, Shanghai 200092, P.R. China

[f.] †These authors contributed equally to this work.

[g.] Correspondence and requests for materials should be addressed to J.H.C. (email: jhchen@uwm.edu).

However, similar sensor performance without probe decoration has not been adequately studied either experimentally or theoretically. In fact, the atomic thickness of 2D nanomaterials presents a system quite sensitive to external electronic perturbations,[40, 41] and the surface-adsorbed positively-charged metal ions not only withdraw charge from the channel material, but also apply an effective gate voltage. Nevertheless, fundamental understanding of the sensing mechanism via the direct interaction between the metal ion and 2D nanomaterial FETs is far from complete. In particular, a rigorous model to quantitatively predict sensor performance and aid in material selection is lacking. Such a quantitative model[42, 43] would not only accelerate the application of FET water sensors by narrowing the searchable phase space for sensing materials, but also reveal new insights into interfacial materials (e.g., membranes, catalysts, etc.) to design novel technologies for addressing energy-water challenges.[44]

Here, we aim to develop a semi-quantitative approach to predict FET sensing performance (e.g., adsorption capacity, sensitivity, and dynamic response range) when metal ions are directly attracted to the surface of 2D nanomaterials by establishing a statistical thermodynamics model with fundamental parameter inputs (e.g., the band gap, the effective mass of the carrier of the sensing material, and the concentration of the target metal ions). Two operating mechanisms (charge transfer vs. gating effect) in the sensor were predicted. To validate the model, 2D nanocrystalline BP nanosheet based FET sensors were selected due to the wide range of band gaps for BP from 2.0 eV for monolayer to 0.3 eV for bulk, which were tested against heavy metal ions such as Hg^{2+}, Pb^{2+}, Cd^{2+}, and Zn^{2+}. We successfully observed the onset and evolution from charge transfer to electrostatic gating as the dominant operating mechanism of BP FET sensors for detecting Hg^{2+} ions in water with high sensitivity and selectivity.

Experimental Methods

Device Fabrication. BP crystals with high purity (> 99.995%) were purchased from HQ Graphene and deposited via micromechanical exfoliation onto degenerately doped <100> Si wafers with a 300 nm-thick thermal oxide. Photoresist was patterned on BP using electron-beam lithography. To make electrical contact with the BP flake, 20 nm of Ni and 40 nm of Au were used as contact metals. After metal deposition using an electron-beam evaporation system, BP served as the conducting channel, bridging the gap of the gold fingers (2 μm). An annealing treatment at 200 °C for 1 h in Ar atmosphere was performed to improve the contact between the BP and gold electrodes. The BP sensor was further identified and confirmed with a Raman spectrometer (Renishaw 1000B). To determine the thickness of the exfoliated BP, AFM was performed using both an Agilent Technology 5420 AFM with a Nanosensors PPP-NCH cantilever, as well as a Bruker Dimension FastScan with ScanAsyst. The electrode regions were encapsulated with polymethyl methacrylate (PMMA), leaving only the sensing region (BP) accessible for the liquid solutions.

Vacuum charge transport measurements. Electrical characterizations of BP devices were performed with a Lakeshore CRX 4K at a pressure of ~10^{-4} Torr, using two Keithley Source Meter 2400 (Keithley, Cleveland, OH) to measure the electrical characteristics of BP at room temperature.

Sensing test. Electrical measurements were performed on BP sensors using a Keithley 4200 semiconductor characterization system. Three-terminal FET measurements were employed for device transport characteristics. Sensor conductance was measured by fixing the drain voltage (V_{DS}) and simultaneously recording the drain current (I_{DS}) when the device was exposed to different concentrations of target ion solutions in PDMS chambers. The metal ions were prepared by diluting the source solutions of $HgCl_2$, $PbCl_2$, $NaCl$, $ZnC_4H_6O_4$, $Cd(NO_3)_2$, and $MgSO_4$ in aqueous environment, respectively. The metal elements are selected so that the electronegativity (the number in the parenthesis) can be arranged in the order of Hg (1.9) > Pb (1.8) > Cd (1.7) > Zn (1.6) > Mg (1.2) > Na (0.9) from the Pauling scale.[45, 46]

Density functional theory calculations. The density functional theory (DFT) calculations were performed by the Quantum Espresso package.[47] The core electrons were treated by the ultra-soft pseudo-potential, while the valence electrons were described by the general gradient approximation of Perdew-Burke-Ernzerhof.[48] The energy and charge density cutoffs were 40 Ry and 480 Ry, respectively. Metal ions were simulated by removing charges from the system and charge redistribution was obtained by solving the Poisson equation. For the metal ion adsorption, a 4×4 supercell of BP was used with the experimental lattice constants (=3.314 Å, b=4.376 Å and c=5.25 Å[49]). The Brillouin zone was sampled by a 16×12×1 Monkhorst-Pack mesh, and a vacuum region greater than 15 Å was used to minimize interactions among the periodic cells. The force criterion for the structural relaxation was 0.02 eV/Å. For the metal ion adsorption calculations, the van der Waals interactions were corrected using the Grimme-D2 method.[50]

Results and discussion

Sensing mechanisms of FET water sensors. An FET water sensor, as depicted in Figure 1A, functions through changes in the drain-source current upon adsorption of metal ions from solution. These adsorbed metal ions on the surface of the sensor affect the electronic properties of the device, causing conductance (current) changes in the sensor. Such interactions between adsorbed metal ions and the sensing material can be categorized into two regimes depending on the specific material and ion concentration investigated, namely, charge transfer and electrostatic gating. Macroscopically, these mechanisms can be described as follows: (1) the positively charged metal ions withdraw electrons from the p-type (n-type) semiconductor upon adsorption leading to a current increase (decrease) due to the increase (decrease) of hole (electron) concentration; and (2) the accumulated positive charges from the metal ions on the surface of the sensor also induce an electrical field, which is equivalent to positive gating and thus further modulates the carrier concentration/mobility, resulting

in a variation of the electrical conductivity in the sensor. As illustrated in Figure 1B, for a p-type semiconductor, these two mechanisms oppose each other: the charge transfer of electrons from the sensor material into the metal ions and the positive gating effect give rise to increase and decrease of current, respectively. These opposing mechanisms necessitate the realization of a theoretical model for qualitative and quantitative understanding of the device performance.

Microscopically, the adsorbed metal ions interact with the sensing material progressively as follows: (1) initially, the metal ions adsorb in an isolated and non-interacting manner and are screened by the sensing material since their spacing d is much
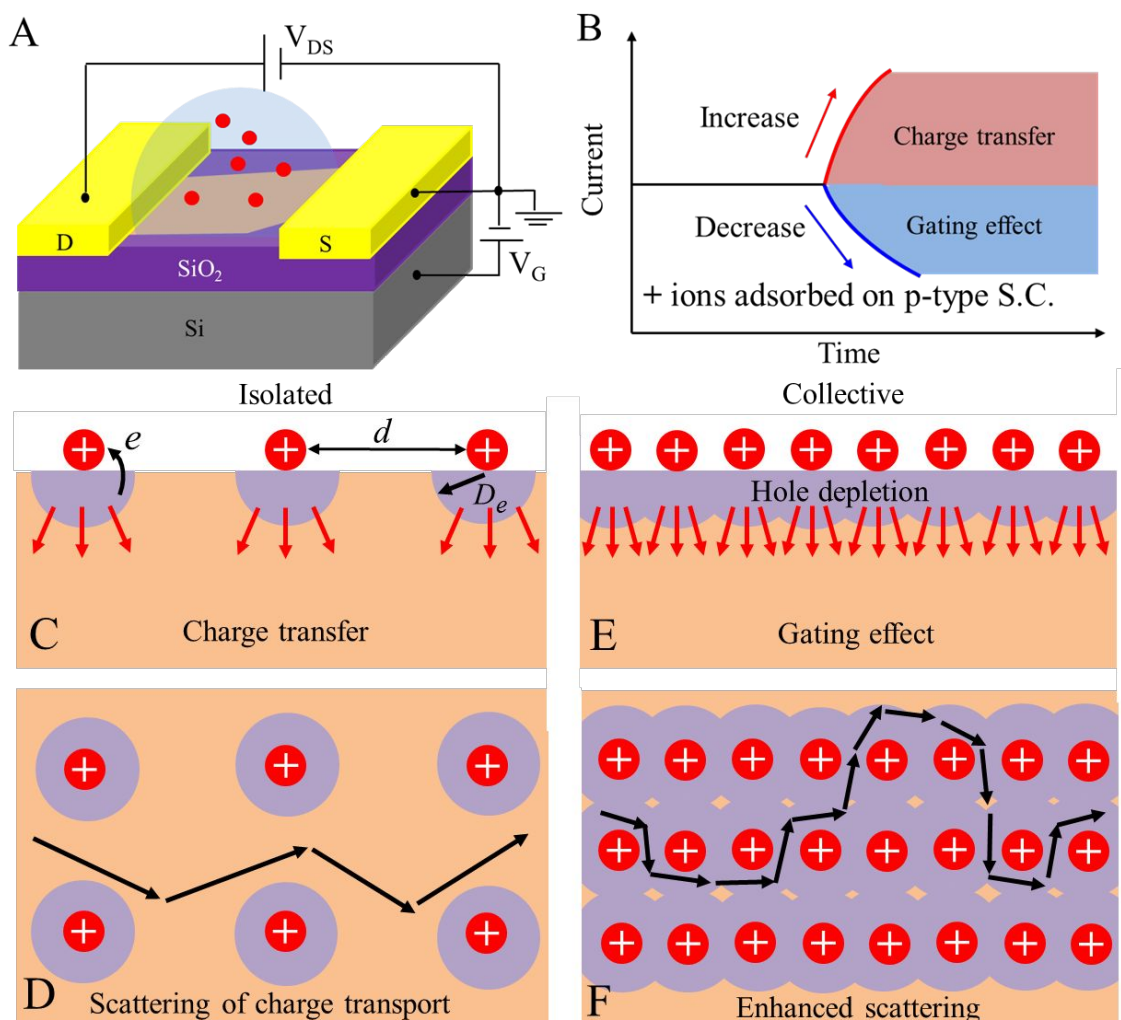
Figure 1. Working principle of an FET water sensor. (A) Device schematic of an FET sensor for the detection of Hg^{2+} ions. (B) Two distinctive mechanisms of current change due to the charge transfer and the gating effect, respectively, when positively charged ions adsorb on the surface of p-type semiconductors. (C-D) and (E-F) are schematics illuminating the sensing mechanisms corresponding to the charge transfer and the gating effect in the side and top views, respectively. e is the charge transfer into a metal ion, d is distance between the surface adsorbed metal ions, and D_e is radius of the Debye sphere (light violet colored region) of the channel material. The red balls represent the positively charged metal ions, while the red arrows depict the lines of electric field from the metal ions, which scatter the charge transport in the underlying channel materials. The black arrows mimic the paths of diffusive transport of charges due to the extrinsic scattering of adsorbed ions.

larger than the Debye length D_e in the sensing material (Figure 1C). Even if the adsorbed ions are still positively charged after withdrawing electrons from a p-type semiconducting sensor material, its effect from the positive electric field on the hole carrier mobility can be largely screened within the Debye sphere in the sensor materials. As a result, the carrier can transport diffusively outside of the Debye sphere (Figure 1D) with negligible mobility degradation and the conductance change in the sensor is dominated by the charge transfer

between the metal ions and the sensing material. (2) When the distance d between the adsorbed metal ions become comparable to and ultimately shorter than the Debye length D_e, the Debye spheres begin to overlap with each other and the metal ions act collectively (Figure 1E). Besides the charge transfer in this case, the accompanying effect is two-fold: on one hand, a hole depletion region around the top surface of the sensor is induced because of the Coulomb repulsion of the positive metal ions, thereby decreasing the hole concentration,

especially in the top region of a thick sensor material; on the other hand, the carrier transport nearby/within the Debye spheres encounters frequent scattering due to the electric field from the positively charged metal ions (Figure 1F), thereby severely degrading the hole mobility. Under such circumstances, the conductance in the sensing material is largely governed by the gating effect.

With the above qualitative analysis of the sensing mechanisms, we further develop statistical thermodynamics models to (semi-)quantitatively characterize the sensor performance in terms of sensitivity and metal ion adsorption density, as revealed in Equation (1)-(4) (supporting information). Eq. (1) defines the sensitivity due to metal ion adsorption-induced relative conductance change in terms of the product of hole concentration (n_h) and mobility (μ) in the sensing material normalized to its initial value $n_{h0}\mu_0$. Upon adsorption, although each metal ion gains Δq_a^+ valence electrons, it retains a net positive charge from $q - \Delta q_g^-$ valence electrons (subscripts a and g indicate the effects of the adsorption-induced charge transfer and gating, respectively), where q is calculations (note that it is not necessary for q to be +2 due to the interaction between the Hg^{2+} ions and the aqueous
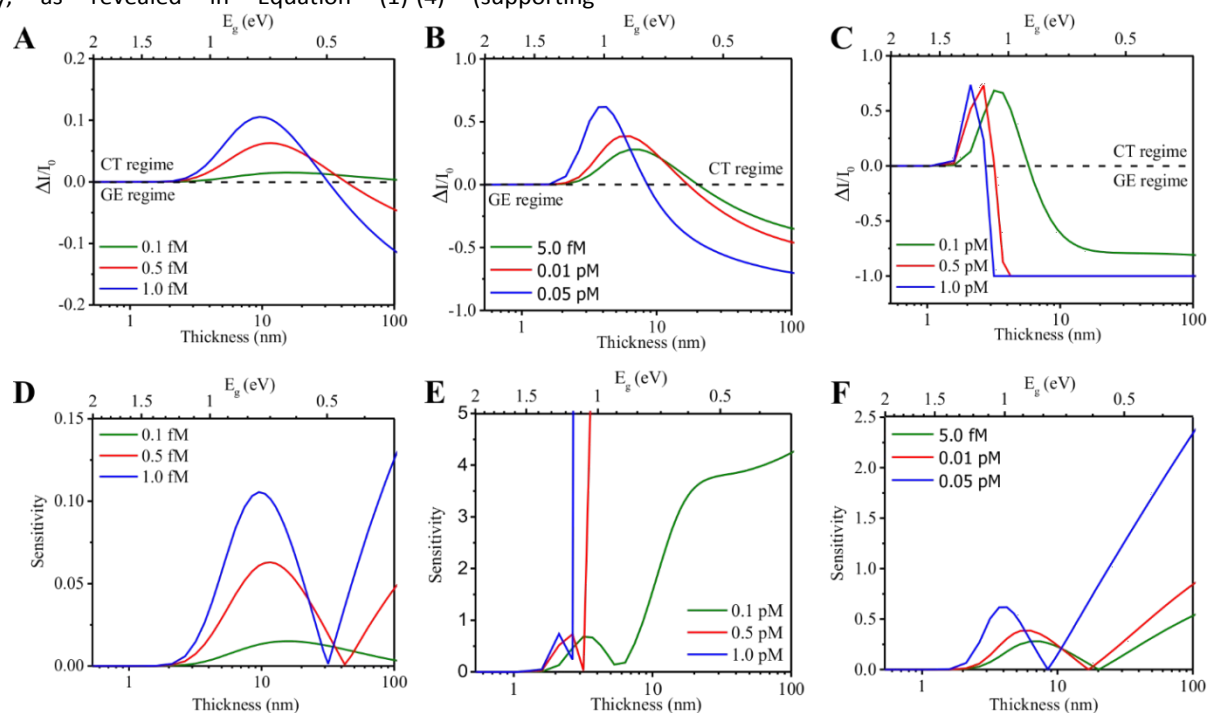
Figure 2. Simulated thickness/band-gap-dependent sensing behavior and sensitivity. (A-C) Simulated normalized current change of BP towards different Hg^{2+} concentrations with respect to BP thickness. The regions of the positive and negative current changes are labeled as the charge transfer (CT) and gating effect (GE) regimes, respectively. (D-F) Simulated sensitivity trends corresponding with (A-C). Here, the sensitivity is defined as $\Delta I/I_0$ and $\Delta R/R_0$ in the CT and GE regimes, respectively.

surroundings). The total charge transfer can be straightforwardly expressed as $n_a\Delta q_a^+$, where n_a is the density of surface-adsorbed metal ions. While this charge transfer elevates the hole concentration, the surface-adsorbed metal ions (still positively charged) decrease hole concentration by effective gating, the magnitude of which depends on the Debye length D_e in the sensing material, the distance d between the adsorbed metal ions, and the empirical parameter α to be determined. Furthermore, the metal ions degrade the hole mobility due to Coulomb repulsion, which is related to D_e, d, and α, as shown in Equation (3). Equation (4) indicates that the metal ion adsorption density n_a is fundamentally controlled by the metal ion concentration (i.e., number density) ρ, thermal wavelength λ, in-plane partition function q_i, Gibbs free energy change ΔE_G after adsorption, and temperature T. Equation (1)-(4) are all dependent on the thickness δ of the sensing material.

$$S = \frac{\Delta I}{I_0} = \frac{n_h\mu - n_{h0}\mu_0}{n_{h0}\mu_0} \tag{1}$$

$$n_h = [n_a\Delta q_a^+ - n_a\Delta q_g^- \, exp\left(-\alpha\frac{d}{D_e}\right)]/\delta + n_{h0} \tag{2}$$

$$\mu = \mu_0[1 - \exp\left(-\alpha\frac{d}{D_e}\right)] \tag{3}$$

$$n_a = \rho\lambda^3\Pi_{i=x,y}q_i\exp\left(-\frac{2\Delta E_G}{k_BT}\right) \tag{4}$$

Although multiple variables are present in our models, they can be reduced to correlate with the intrinsic parameters of the sensing material (e.g., band gap and carrier mobility) and the metal ion concentration. Due to its tunable band gap, we designed a BP nanosheet FET sensor for detecting Hg^{2+} ions. Figure 2A-C show the simulated normalized current changes $\Delta I/I_0$ with respect to the thickness/band gap of a BP sensor as a function of Hg^{2+} concentrations from 0.1 fM to 1.0 pM. Overall, the current change $\Delta I/I_0$ first increases to a maximum ($\Delta I/I_0$|max) before decreasing to negative values, corresponding with charge transfer dominating transport and the gating effect being dominant, respectively. Specifically, at

the extremely low Hg^{2+} ion concentration of 0.1 fM, the current change is positive irrespective of the thickness (i.e., band gap) of the BP due to the large distance between the adsorbed Hg^{2+} ions at this non-interacting limit, as demonstrated in Figure 1 C,

D. Beyond 0.1 fM, $\Delta I/I_0$ starts to become negative when the thickness (band gap) is larger
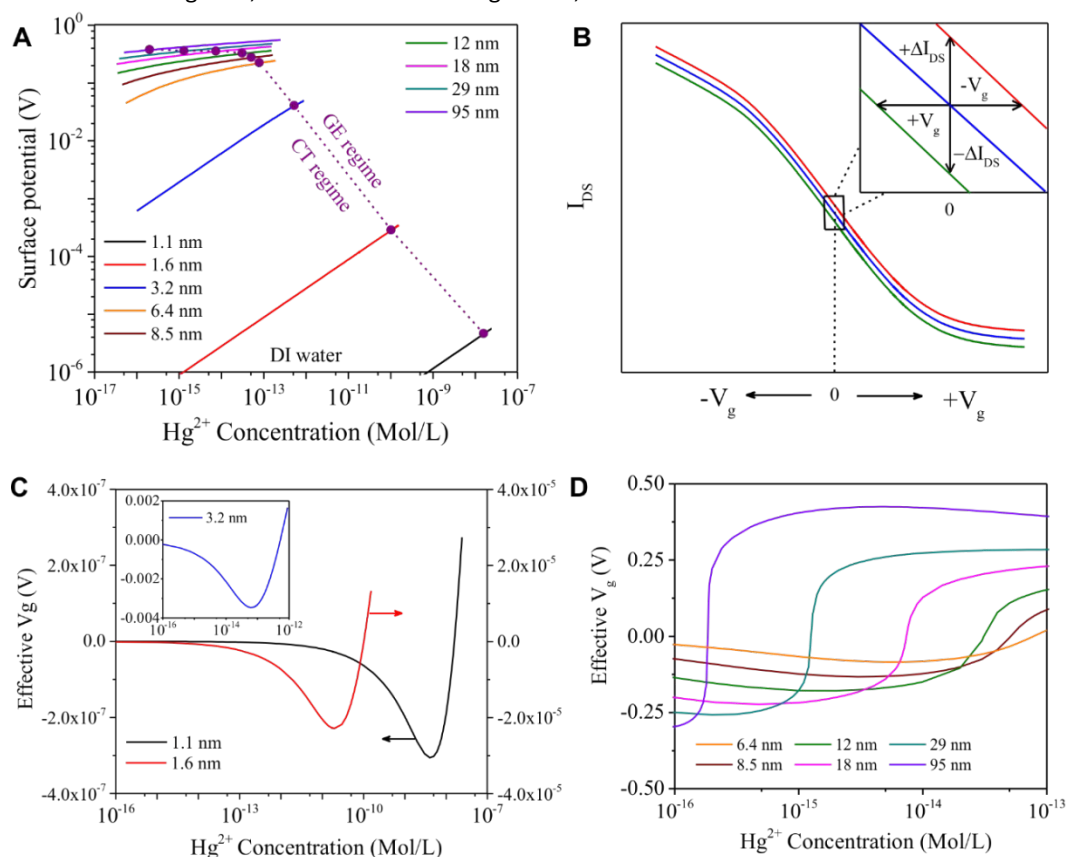
Figure 3. Simulated mercury ion adsorption-induced surface potential/effective gate voltage. (A) Surface potential change with respect to the concentration of Hg^{2+} ions for various thicknesses of BP. The dotted line indicates the transition from the charge transfer regime into the gating effect regime at the critical Hg^{2+} ion concentration. (B) Illustration of the drain-source current I_{DS} tuning in an FET device by the external gate voltage, where the inset demonstrates the decrease/increase of I_{DS} due to an effective positive/negative gate voltage. (C-D) The effective gate voltage V_g as a function of the Hg^{2+} ion concentration for different thicknesses of BP corresponding with those in (A).

(smaller) than a critical value, a trend that is more pronounced at higher Hg^{2+} concentrations. The competition between the charge transfer and the gating effect in Figure 2 A-C implies that both can be adopted for sensitivity modulation by engineering the thickness/band gap for a target Hg^{2+} concentration, as evidenced in Figure 2 D-E. For example, charge transfer can be employed for thinner (i.e., larger band gap) BP, while the gating effect can be employed for thicker (i.e., smaller band gap) BP. For both cases, the sensitivity can be maximized by fine-tuning the thickness/band gap. Moreover, thinner/thicker (larger/smaller band gap) BP is more suitable for detecting Hg^{2+} ions at lower/higher response range by designing rational arrays of BP with different thicknesses.

Although charge transfer and gating effects are used to distinguish the different current modulation trends in Figure 2, it should be noted that these two concepts can be inherently related. Physically, the surface-absorbed Hg^{2+} ions exert a

positive potential on the underlying BP. Using the Grahame equation within the framework of an electrostatic double-layer model,[51] Figure 3A shows that this surface potential increases as the Hg^{2+} ion concentration increases and the gating effect occurs only when the surface potential (or the Hg^{2+} ion concentration) reaches a critical value. Typically, the transfer characteristics curve for a p-type semiconductor (illustrated in Figure 3B) suggests that the applied positive (negative) surface potential decreases (increases) the drain-source current. This result implies that the charge transfer in Figure 2 is essentially equivalent to a negative gate voltage. Generally, only the carrier concentration is tuned without the change in mobility by the gate voltage in a very narrow range around 0. Given the small values shown in Figure 3A, the surface potential thereafter can be converted into an effective gate voltage V_g by considering the effects of both carrier degradation and hole

Journal Name
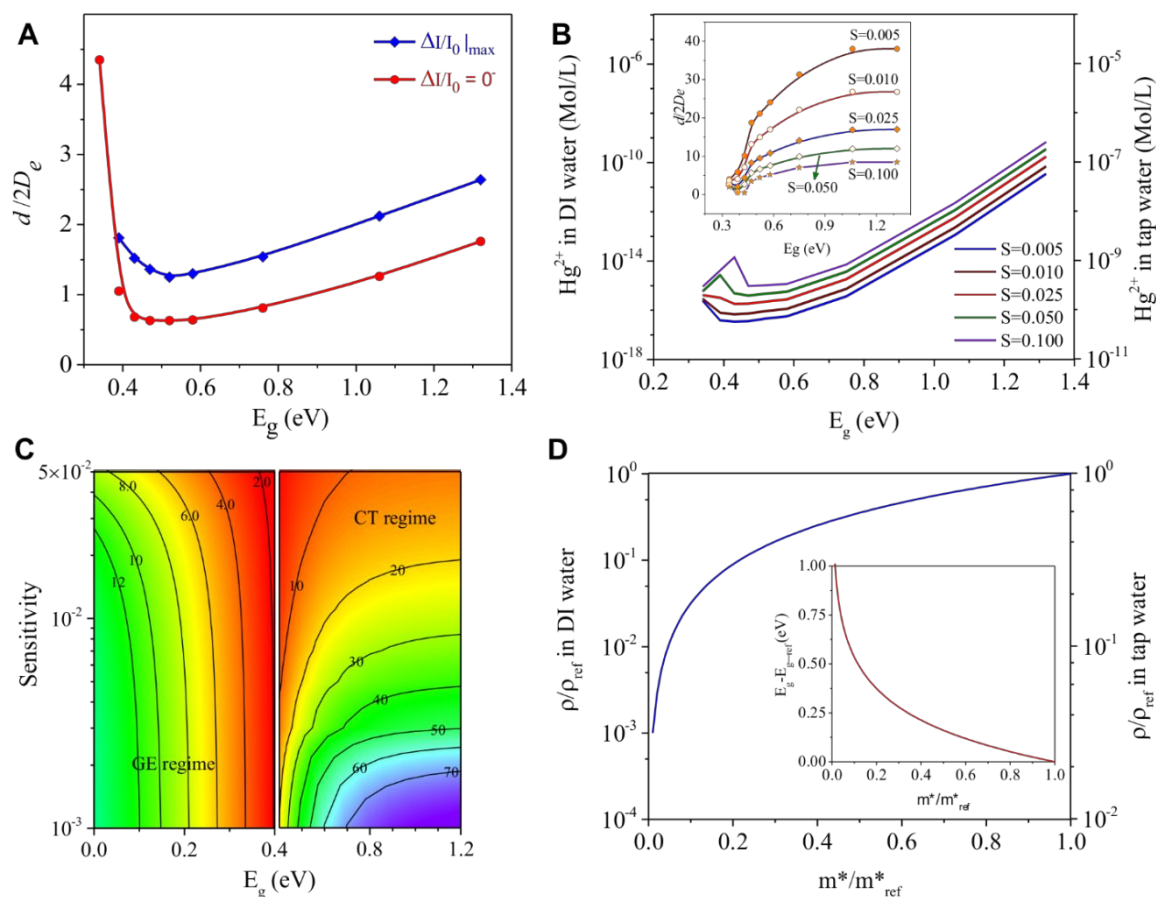
Figure 4. Relationship between the Debye length D_e and the sensing mechanism. (A) The variation of the ratio between the half distance $d/2D_e$ of adsorbed Hg^{2+} ions and the Debye length D_e as a function of the band gap in BP when $\Delta I/I_0$ is maximized in the CT regime and is 0^-, respectively. (B) The detected concentration of Hg^{2+} ions with respect to the band gap E_g of BP at different sensitivities in DI water (left axis) and tap water (right axis), respectively. The inset shows the trend of $d/2D_e$ with respect to E_g at the sensitivities corresponding with those in (B). (C) Colored contour map of $d/2D_e$ with respect to both E_g and the sensitivity in the gating effect regime (left panel) and charge transfer regime (right panel), respectively. The numbers in the solid lines are the isovalues of $d/2D_e$. (D) Relationship between the detectable Hg^{2+} ion concentration and the effective mass of carriers in the DI water (left axis) and tap water (right axis), respectively. The inset shows the relationship between the band gap and the effective mass of carriers for detecting Hg^{2+} ions at the same concentration with the same sensitivity.

concentration tuned by the adsorbed Hg^{2+} ions. Figure 3 C-D present the effective gate voltage with respect to the Hg^{2+} ion concentration for different thicknesses of BP. Evidently, this effective gate voltage is negative (positive) at low (high) Hg^{2+} ion concentrations, and the amplitude of negative gate voltage first increases and then decreases as the Hg^{2+} ion concentration increases, consistent with the current change in Figure 2. We also see that the adsorbed Hg^{2+} ions-induced gate voltage is relatively small (< 0.5 V), indicating the sensitive control of the carrier concentration in 2D nanomaterials by metal ions.

Guidelines for the quantitative design of sensors for Hg^{2+} ion detection. As revealed in our models, the sensing mechanism of either the charge transfer or gating effect is controlled by how the distance between the adsorbed ions evolves with respect to the Debye length in the sensor materials. For a definitive distinction, we identified the criteria by quantitatively

correlating the ratio of the half distance $d/2$ over the Debye length D_e with the two mechanisms. Figure 4A presents the ratio $d/2D_e$ with respect to the band gap of BP when the current change is maximized and decreases to 0^- (the minus sign indicates the negative direction of the current change). Interestingly, this ratio first decreases and then increases as the band gap increases for both cases in a similar manner. We further obtained the values of the ratio $d/2D_e$ and the corresponding band gap by varying the Hg^{2+} concentrations (Figure S1). For both $\Delta I/I_0|_{max}$ and $\Delta I/I_0 = 0^-$, the ratio $d/2D_e$ decreases and the corresponding band gap increases as the Hg^{2+} concentration increases. Physically, larger values of $d/2D_e$ suggest that the sensor material is more perturbed by external scattering; in other words, the gating effect impacts sensor performance more strongly for BP flakes with either extreme thickness or thinness (larger and smaller band gap) due to the

adsorbed ions, as shown in Figure 4A, and for lower Hg^{2+} concentrations, as shown in Figure S1.

Apart from the differentiation between the charge transfer and the gating effect, $d/2D_e$ also reflects a measure of the sensitivity. For example, the inset in Figure 4B shows the trends of $d/2D_e$ with respect to the band gap E_g at several sensitivities. We see that different values of $d/2D_e$ correspond with a specific sensitivity and band gap, indicating that the sensitivity can be obtained once the values of $d/2D_e$ and E_g are known. On one hand, the detectable Hg^{2+} ion concentration is smallest when E_g is ~0.4 eV, consistent with the trends of $d/2D_e$ in Figure 4A and the inset of Figure 4B, and suggesting that the lowest detection limit of Hg^{2+} ions in deionized (DI) water can be achieved when the band gap of BP is ~ 0.4 eV; on the other hand, the correspondence between $d/2D_e$, the band gap E_g, the sensitivity S, and the ion concentration ρ implies that each of them can be inferred when the other three are known. For the purpose of future sensor design and material selection, it is a priority to predict the lower detection limit of Hg^{2+} ions from the candidate materials.

To this end, we derive from our model that

$$\rho^{\frac{1}{2}} = \frac{4\pi^2 e k_B T (m_e m_p)^{\frac{3}{4}}}{h^3 \sqrt{\varepsilon_0}\sqrt{\prod_{i=x,y} q_i}} \cdot \frac{(zm_h^*)^{\frac{3}{4}}}{\frac{d}{2D_e}\sqrt{\varepsilon}} \exp\left[\frac{4\Delta E_G - E_g - 2(E_F - E_{Fi})}{4k_B T}\right] \qquad (5)$$

where $e, k_B, T, m_e(m_p), h, \varepsilon_0, z, m_h^*, E_F(E_{Fi})$ are the elementary charge, Boltzmann constant, temperature, mass of an electron (proton), Planck's constant, vacuum permittivity, atomic weight number of metal ion, effective mass of hole, Fermi level (intrinsic one), respectively. For Hg^{2+} ions at 300 K, Equation (5) then reduces to

$$\rho[\text{Mol/L}] = 0.744 \times 10^{-14} \cdot \frac{\varepsilon^{-1} m_h^{*\frac{3}{2}}}{\left(\frac{d}{2D_e}\right)^2} \cdot \exp\left[\frac{E_g - 6(E_F - E_{Fi})}{0.155\text{eV}}\right] \qquad (6)$$

From Equation (6), we can see that the detectable concentration of Hg^{2+} ions depends on two sets of parameters: the intrinsic properties of BP (e.g., $\varepsilon, m_h^*, E_g, E_F, E_{Fi}$) and $d/2D_e$. While these intrinsic properties can be readily obtained using state-of-the-art first-principles calculations,[36, 52] $d/2D_e$ relates to both the sensitivity S and the band gap E_g (Figure S2). The energy spacing between the Fermi levels in Equation (5) and (6) can be described by the carrier concentration, namely, $\exp\left[-(E_F - E_{Fi})/k_B T\right] = \sqrt{n_h/n_e}$ for p-type semiconductors, where n_h and n_e are the hole and electron concentrations, respectively. As seen from Figure 4B that the transition between the charge transfer and the gating effect mechanism occurs at the band gap of ~0.4 eV irrespective of sensitivity, we thus treat them separately. For the purpose of quantitatively estimating of the lower detection limit, small values of S are reasonable and limited to below 0.05 here. We fit $d/2D_e$ with respect to E_g and S in the charge transfer and gating effect regimes in the DI water, respectively, and obtain

$$\frac{d}{2D_e}\bigg|_{0 < S \leq 0.05} = \begin{cases} 2.8\exp\left(-\frac{0.07}{E_g^{3.34}}\right)S^{-\frac{1}{2}}, & E_g \geq 0.4[\text{eV}] \\ (15 - 32E_g) - (125 - 285E_g)S, & 0 < E_g \leq 0.4[\text{eV}] \end{cases} \qquad (7)$$

Figure 4C presents the color map of $d/2D_e$ with respect to E_g and S using Equation (7). The isolines show that $d/2D_e$ decreases (increases) when E_g increases (decreases) concurrently with S in the charge transfer and gating effect regimes, respectively, in agreement with the inset of Figure 4B. Equation (6) and (7) enable us to predict the detectable concentration of Hg^{2+} ions when the intrinsic properties of a crystalline semiconductor are known. We also can see from Equation (6) that a lower detection limit (large band gap) can be achieved (allowed) for smaller effective mass of the carriers (i.e., larger carrier mobility) in the selection of candidate sensor materials (Figure 4D).

Armed with the results above, we further extend Equation (6) to the case of tap water with various ionic constituents which, in contrast to DI water, inevitably affect the Hg^{2+} ion adsorption. The effects in tap water are essentially two-fold: (1) On one hand, the Na^+ ions compete with the Hg^{2+} ions for adsorption while the adsorbed Hg^{2+} ion density n_a' in tap water now is $n_a \rho_{Hg^{2+}}/\rho_{Na^+}$ within the framework of an ideal gas mixture model.[53] This is reasonable for very small ρ_{Na^+} (on the order of 10^{-4} Mol/L in tap water) since the ionic interaction among the ions can be neglected. (2) On the other hand, because the working range of the gating effect is limited by the Debye length of the ion solutions,[54-56] the surface-adsorbed Hg^{2+} ions are thus screened by the stray ions in the tap water (e.g., Na^+, Cl^-, and the Debye screening length D_e is ~30 nm). Consequently, the effective Debye length can be expressed as $D_e'^{-1} = D_e^{-1} + \lambda_D^{-1}$, where $\lambda_D = \sqrt{\varepsilon_{H_2O} k_B T / e^2 \sum_i \rho_i z_i^2}$ is the Debye length in tap water (~30 nm at 300 K). Using Equation (4) and (6), we have

$$\rho[\text{Mol/L}] = (0.744 \times 10^{-14}\rho_{Na^+})^{\frac{1}{2}} \cdot \frac{\varepsilon^{-\frac{1}{2}} m_h^{*\frac{3}{4}}}{\frac{d}{2D_e'}} \cdot \exp\left[\frac{E_g - 6(E_F - E_{Fi})}{0.31\text{eV}}\right] \qquad (8)$$

$$\frac{d}{2D_e'} = \frac{d}{2D_e}\left\{1 + \exp\left[\frac{E_g + 2(E_F - E_{Fi})}{4k_B T}\right] \cdot \left[\frac{1}{2}\left(\frac{h^2}{2\pi m_h^* m_e k_B T}\right)^{\frac{3}{2}}\sum_i \rho_i z_i\right]^{\frac{1}{2}} \cdot \left(\frac{\varepsilon}{\varepsilon_{H_2O}}\right)^{\frac{1}{2}}\right\}$$

$$(9)$$

where ρ_i and z_i are the concentration of ion species i and its valence charge, respectively, and ε_{H_2O} is the relative permittivity of water. Compared with Equation (6), Equation (8) reveals that both the detectable Hg^{2+} ions and the effect of m_h^* are degraded by the Na^+ ions (Figure 4B and Figure 4D).

Simulated and experimental dynamic responses towards Hg^{2+} ions. Figure 5A shows the simulated normalized current change $\Delta I/I_0$ at the equilibrium state with respect to Hg^{2+} ion concentrations for BP nanosheets with various thicknesses in DI water. Similar to the current change as a function of BP thickness at certain Hg^{2+} ion concentrations in Fig.2, we observe the onset and evolution from charge transfer to gating effect. Figure 5B and C present the simulated dynamic responses with several Hg^{2+} ion concentrations for BP with selected thicknesses

in Figure 5A, which suggests that thinner BP responds faster than thicker BP at the same Hg^{2+}
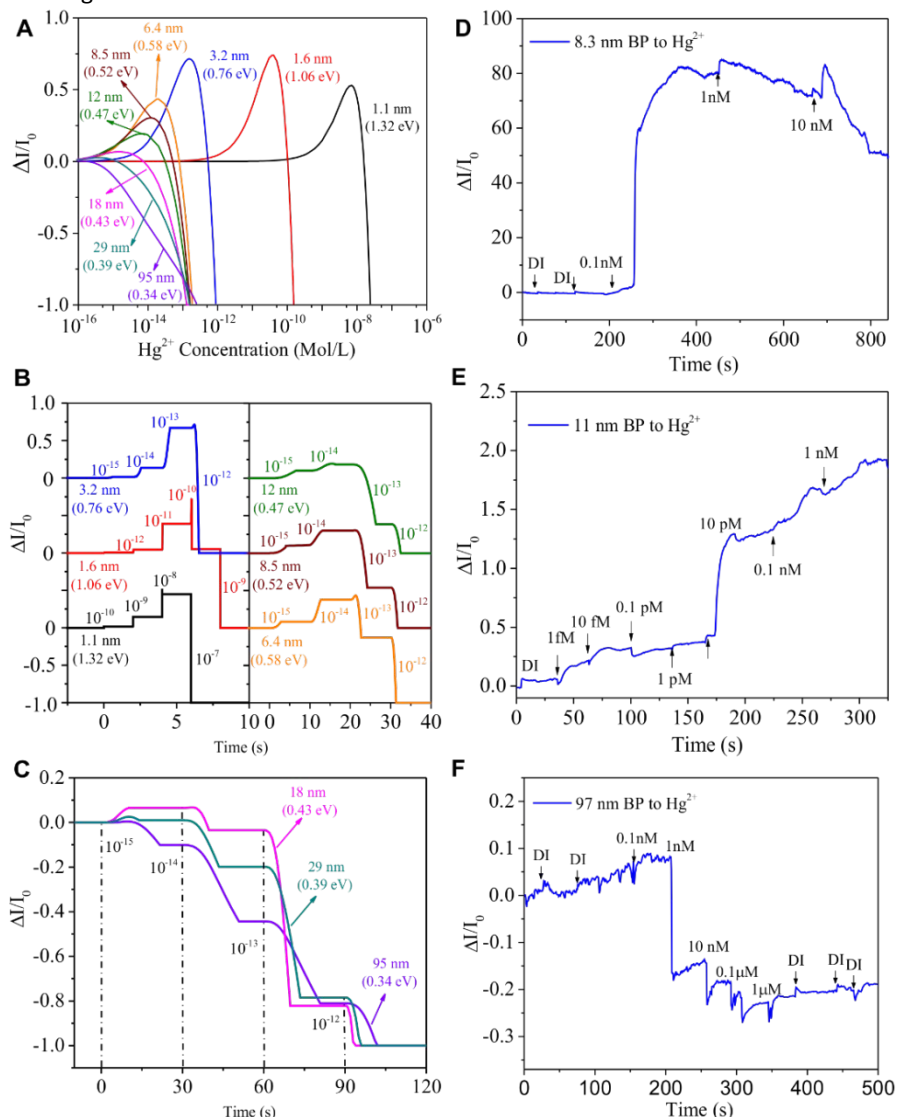
Figure 5. Real-time sensor performance from modeling and experiments in DI water. (A) Simulated normalized current change of BP towards Hg^{2+} at different BP thicknesses; (B-C) Simulated dynamic responses with respect to Hg^{2+} concentration (in Mol/L, 10^{-9} Mol/L=0.2 ppb), with the BP thicknesses corresponding with those in (A) but with the same sensor area (10 μm^2). The short dashed lines in (C) indicate the beginning of drop-casting Hg^{2+} ion solutions. The time duration of all Hg^{2+} concentrations is set to 2.5, 10, 30 s in the left, right panel in (B) and in (C), respectively, so that the Hg^{2+} ion adsorption reaches the equilibrium state at each concentration. (D-F) Experimental dynamic responses to Hg^{2+} at varying concentrations for BP with thicknesses of 8.3 nm, 11 nm, and 97 nm in (D), (E), and (F), respectively. The source-drain voltage V_{DS} was kept at 0.01 V to maintain the device stability for operation under aqueous conditions; a higher voltage could lead to significant Joule heating that would result in signal drift.

concentration (ranging from 4.5 ms for 1.1 nm-thick BP to 21.6 s for 95 nm-thick BP, also *cf*. Figure S3. The response time is independent of ion concentration and is related only to the band gap and surface area of the sensor material itself). This is expected since fewer Hg^{2+} ions are needed to reach the adsorption equilibrium for thinner, smaller BP flakes. Figure 6A and B further show the current change at equilibrium with respect to the Hg^{2+} ion concentrations and the simulated dynamic responses of BP at different thicknesses in tap water,

respectively. In contrast to Figure 5A-C, the stray ions (e.g., Na$^+$, Cl$^-$) in tap water screen the gating effect of absorbed Hg^{2+} ions and enhance current change, especially for thinner BP. The lower detection limit also increases from ~0.1 fM in DI water to 0.1 nM in tap water.

To validate the simulated sensor behaviors shown in Figure 5A-C and Figure 6A-B, BP nanosheet FET sensors with different BP thicknesses were fabricated (Figure S4). The output and transfer characteristics of the as-fabricated sensors were first

Journal Name

ARTICLE
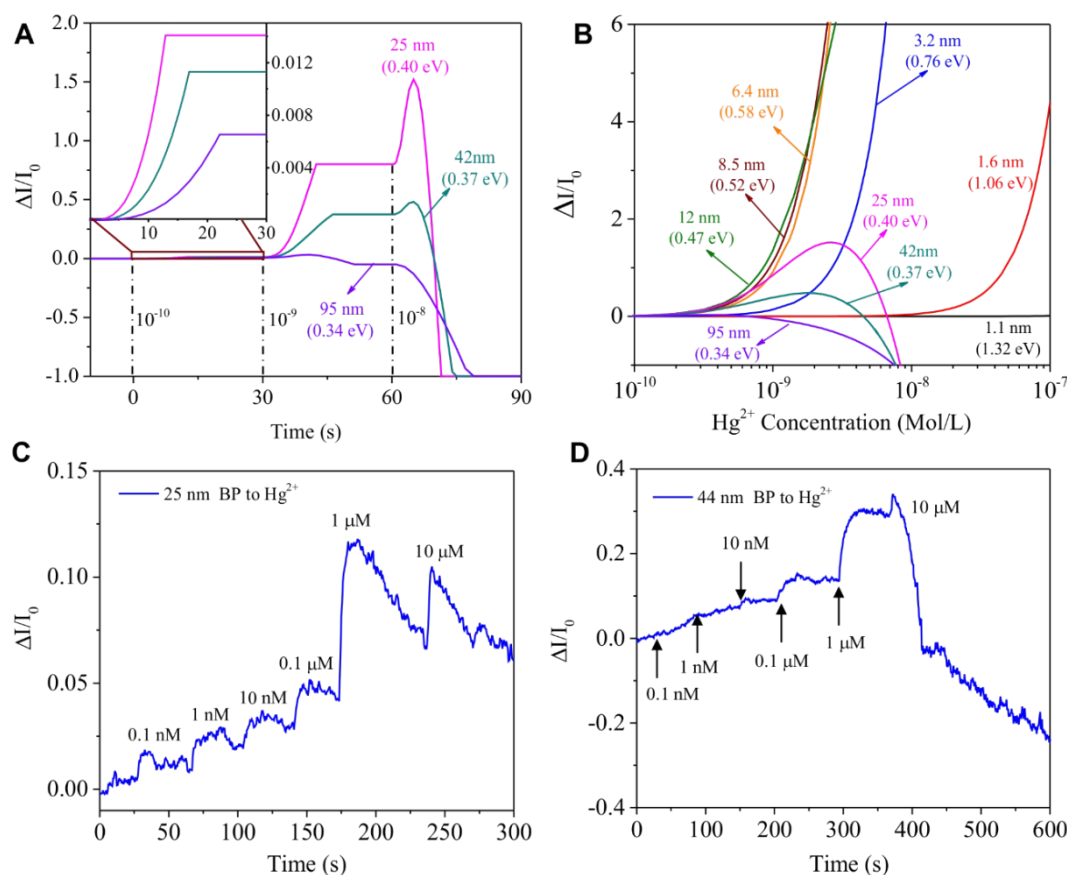
Figure 6. Real-time sensor performance from modeling and experiments in tap water. (A) Simulated normalized current change of BP towards Hg^{2+} at different BP thicknesses; (B) Simulated dynamic responses with respect to Hg^{2+} concentration with the time duration of 30s and the sensor area of 10 μm^2. The short dashed lines indicate the beginning of drop-casting of Hg^{2+} ion solutions. The inset is the magnified view of the dynamic response from 0 to 30s. (C-D) Experimental dynamic responses to Hg^{2+} at varying concentrations for BP with thicknesses of 25 nm, and 44 nm in (C), and (D), respectively.

measured to confirm the BP/electrode contact quality and the FET properties required for good sensor performance (Figure S5). The sensors were then tested against various Hg^{2+} ion concentrations diluted in DI (pH=7.8) /tap water (pH=8.0). Figure 5D presents the dynamic response of an 8.3 nm-thick BP sensor in DI water. The current increases dramatically (by almost 80 times) when exposed to 0.1 nM Hg^{2+} due to the charge transfer from the p-type BP into Hg^{2+} ions. However, the current starts to decrease at higher concentrations (1 nM and 10 nM Hg^{2+}), indicating that the gating effect begins to prevail over the charge transfer effect. To further verify the charge transfer and the gating effect, an 11 nm-thick BP sensor and a 97 nm-thick BP sensor were tested against Hg^{2+} in DI water but with concentrations starting from 1fM and 0.1 nM, as shown in Figure 5E and F, respectively. The charge transfer effect can still be observed when the Hg^{2+} concentration is increased from 1 fM to 1 nM (Figure 5 E). Even though the current increased only slightly at 0.1 nM Hg^{2+}, indeed we observe from Figure 5F that

the current dropped at 1 nM Hg^{2+} and started to saturate beyond 10 nM Hg^{2+}. In contrast, the experimental dynamic responses in tap water shown in Figure 6C-D reveal that the current increases, even when starting from 0.1 nM Hg^{2+} ions, while the gating effect occurs only at very high Hg^{2+} ion concentrations.

Our models suggest that the carrier effective mass (i.e., carrier mobility) and band gap are the two most important and directly relevant selection criteria of the channel material for optimizing sensor performance. By directly correlating the metal ion adsorption capacity with the metal ion concentration our models additionally offer insights into designing future sensors by manipulating the band gap (or thickness) of 2D-layered semiconductors. The models established here for BP-based FET water sensors are also broadly applicable to other p-type semiconducting nanomaterials and can be further extended to other n-type semiconductors by replacing the hole-related parameters (m_h^*, n_h) with electron-related parameters

(m_e^*, n_e) and by replacing the energy spacing term $E_F - E_{Fi}$ by $E_{Fi} - E_F$, respectively. Equation (6) and (8) suggest that a lower detection limit could be achieved by using materials with lower initial doping concentration as compared with heavily doped semiconductors with identical band gap, carrier mobility, and dielectric constant.

From the material side, due to both the electronic properties of BP and the moderate oxidizing ability of Hg^{2+} ion (Figure S6), BP is both ultrasensitive and uniquely selective to Hg^{2+} ions without the specific probe decoration compared with other metal ions (Pb^{2+}, Cd^{2+}, Zn^{2+}, Mg^{2+}, *cf.* Figure S7). As seen in Figure 5 and Figure 6, the experimental lower detection limit can fall as low as 1fM/0.1nM in DI and tap water, respectively, much lower than the maximum contaminant level for Hg^{2+} ions in tap water (9.9 nM) recommended by the U.S. Environmental Protection Agency. This is superior to most of the current sensor technologies for detecting Hg^{2+} ions. For example, the standard inductively coupled plasma mass spectrometry, colorimetric gold nanoparticle-based optical sensors, DNA-grafted graphene electrochemical biosensors, organic polymer-based FET sensors, and MoS_2-based FET sensors have been developed for Hg^{2+} ions but with lower detection limits of 0.25 nM,[57] 50 nM,[58] 5 nM,[59] 10 mM,[28] and 30 pM,[27] respectively, while only the graphene-based aptasensor had an extremely lower detection limit of 10 pM.[22]

However, it should be noted that BP is unstable in an aqueous environment when oxygen is present [60-63] (Figure S8 and S9). Moreover, Edmonds and Fuhrer *et al.* found that the intermediate oxide P_4O_2 occurs before evolving into the phosphorus pentoxide P_2O_5;[64] therefore, BP is more likely to be only locally oxidized into P_4O_2 in an aqueous environment during the short period of our sensing tests (several minutes). This surface oxidation effectively increases the band gap (ΔE_g) of BP and thus shifts the lower detection limit to the higher concentration. In other words, the surface oxidation degrades sensor performance, and the degradation grows rapidly by a quantitative degree of $\sim\exp(\Delta E_g/6k_BT)$. For example, the theoretical lower detection limit of $\sim$0.5 fM for 6 nm-thick BP (Figure 2 and Figure 5) could be magnified by a factor of $\sim$2×10^3 into 1 pM at ΔE_g of 1.18 eV, which is comparable to the experimental lower detection limit of $\sim$1 pM for 6.0 nm BP (Figure S8). This is reasonable for the locally oxidized BP at the early stage, since the band gap could be as large as 3.35 eV, even for the intermediate oxidation.[65] Consequently, BP could be a promising candidate once it is protected against surface oxidation, but without affecting the direct contact between BP and Hg^{2+} ions, e.g., ionophore passivation to elongate the life time as demonstrated by Li and Zhang *et al.*[66] for detecting Pb^{2+} ions using BP. Covalent modification chemistries for BP that saturate phosphorus lone pairs may also be useful in this regard.[67]

Conclusions

In summary, an FET water sensor for metal ion detection works in the charge transfer and gating effect regimes at low and high concentrations of ions, respectively. Here, a theoretical methodology is provided to semi-quantitatively describe the metal ion adsorption density, sensitivity, lower detection limit, and description of the dynamic response behaviour of FET water sensors when intrinsic properties of the sensor material and the concentration of the target metal ions are known. In addition, due to its moderate oxidizing ability, Hg^{2+} ions are ideal for probe-free detection by 2D crystalline nanomaterials with a suitable band gap. We validated that BP nanosheet FET sensors without any probe decoration are highly sensitive to Hg^{2+} ions with a fast response and an excellent lower detection limit. Our models, generic to all 2D semiconducting nanomaterials, offer insights into the mechanism of FET water sensors and provide guidelines for the quantitative molecular design of future sensor systems with optimized performance. The superior performance of BP nanosheet FET water sensors also suggest opportunities for early warning in smart water distribution systems.

Supporting Information

Relationship between $d/2D_e$ and Hg^{2+} concentrations (Figure S1), the ratio $d/2D_e$ with respect to the sensitivity (Figure S2), the predicted dynamic response time of BP with respect to its thickness for different BP surface areas (Figure S3), multilayer BP-based FET sensor and its structural characterization (Figure S4), the output and transfer characterization of BP sensor (Figure S5), adsorption of Hg^{2+} ions on BP (Figure S6), selectivity of BP sensor (Figure S7), dynamic response to Hg^{2+} ion with varying concentrations at a BP thickness of 6.0 nm (Figure S8), dynamic response to Hg^{2+} ion with varying concentrations at a BP thickness of 4.2 nm (Figure S9), the binding energy E_b of Hg^{2+} with respect to the number n of water molecules on phosphorene (Figure S10), the Debye screening length of BP as a function of BP thickness (Figure S11), schematic of the region in the droplet of Hg^{2+} solution within which the Hg^{2+} ions diffuse and adsorb on the surface of BP (Figure S12), supplementary methods, and supplementary references.

ACKNOWLEDGMENTS

high-performance computation center at the University of Wisconsin-Milwaukee.

Conflicts of interest

There are no conflicts to declare.

References

1. C. T. Driscoll, R. P. Mason, H. M. Chan, D. J. Jacob and N. Pirrone, *Environ. Sci. Technol.*, 2013, **47**, 4967-4983.
2. E. B. Swain, D. R. Engstrom, M. E. Brigham, T. A. Henning and P. L. Brezonik, *Science*, 1992, **257**, 784-787.
3. S. Bolisetty and R. Mezzenga, *Nat. Nanotechnol.*, 2016, **11**, 365–371.
4. M. Podar, C. C. Gilmour, C. C. Brandt, A. Soren, S. D. Brown, B. R. Crable, A. V. Palumbo, A. C. Somenahally and D. A. Elias, *Sci. Adv.*, 2015, **1**, e1500675.
5. T. A. Saleh, M. Tuzen and A. Sari, *J. Environ. Manage.*, 2018, **211**, 323-333.
6. T. A. Saleh, *Environ. Sci. Pollut. Res.*, 2015, **22**, 16721-16731.
7. T. A. Saleh, *J. WATER SUPPLY RES. T.* , 2015, **64**, 892-903.
8. A. Giang and N. E. Selin, *Proc. Natl. Acad. Sci. USA*, 2016, **113**, 286-291.
9. S. D. Emslie, R. Brasso, W. P. Patterson, A. Carlos Valera, A. McKenzie, A. Maria Silva, J. D. Gleason and J. D. Blum, *Sci. Rep.*, 2015, **5**, 14679.
10. S. R. Rieder, I. Brunner, O. Daniel, B. Liu and B. Frey, *Plos One*, 2013, **8**, e61215.
11. S. A. AL-Hammadi, A. M. Al-Amer and T. A.Saleh, *Chem. Eng. J*, 2018, **345**, 242-251.
12. T. A. Saleh, *Advanced Nanomaterials for Water Engineering, Treatment, and Hydraulics*, IGI Global, 2017.
13. T. A. Saleh and V. K. Gupta, *Nanomaterial and Polymer Membranes*, Elsevier, 2016.
14. T. A. Saleh, *Desalin. Water Treat.*, 2015, **57**, 10730-10744.
15. J. B. Chang, G. H. Zhou, E. R. Christensen, R. Heideman and J. H. Chen, *Anal. Bioanal. Chem*, 2014, **406**, 3957-3975.
16. E. J. Kim, B. H. Chung and H. J. Lee, *Anal. Chem.*, 2012, **84**, 10091-10096.
17. H. H. Lou, Y. Zhang, Q. Xiang, J. G. Xu, H. Li, P. C. Xu and X. X. Li, *Sensor Actuat. B-Chem.*, 2012, **166**, 246-252.
18. D. F. Lu, J. Y. Li and Z. M. Qi, *J. Appl. Phys.*, 2013, **113**, 213109.
19. R. Wang, W. Wang, H. Ren and J. Chae, *Biosens. Bioelectron.*, 2014, **57**, 179-185.
20. N. Yildirim, F. Long, M. He, C. Gao, H. C. Shi and A. Z. Gu, *Talanta*, 2014, **129**, 617-622.
21. A. Senthamizhan, A. Celebioglu and T. Uyar, *Sci Rep*, 2015, **5**, 10403.
22. J. H. An, S. J. Park, O. S. Kwon, J. Bae and J. Jang, *ACS Nano*, 2013, **7**, 10563-10571.
23. T. Luo, M. He, C. Gao, J.-H. Liu and X.-J. Huang, *Electrochem. commun.*, 2014, **42**, 26-29.
24. S. Yang, D. Meng, J. Sun, W. Hou, Y. Ding, S. Jiang, Y. Huang, Y. Huang and J. Geng, *RSC Adv.*, 2014, **4**, 25051-25056.
25. Y. Zhang, G.-M. Zeng, L. Tang, Y.-P. Li, Z.-M. Chen and G.-H. Huang, *RSC Adv.*, 2014, **4**, 18485-18492.
26. S. Mao, J. B. Chang, G. H. Zhou and J. H. Chen, *Small*, 2015, **11**, 5336-5359.
27. S. Jiang, R. Cheng, R. Ng, Y. Huang and X. Duan, *Nano Res.*, 2015, **8**, 257-262.
28. O. Knopfmacher, M. L. Hammock, A. L. Appleton, G. Schwartz, J. G. Mei, T. Lei, J. Pei and Z. N. Bao, *Nat. Commun.*, 2014, **5**.
29. S. Lei, X. Wang, B. Li, J. Kang, Y. He, A. George, L. Ge, Y. Gong, P. Dong, Z. Jin, G. Brunetto, W. Chen, Z.-T. Lin, R. Baines, D. S. Galvão, J. Lou, E. Barrera, K. Banerjee, R. Vajtai and P. Ajayan, *Nat. Nanotechnol.*, 2016, **11**, 465–471.
30. D. Sarkar, X. Xie, W. Liu, W. Cao, J. Kang, Y. Gong, S. Kraemer, P. M. Ajayan and K. Banerjee, *Nature*, 2015, **526**, 91-95.
31. M. Lukas, V. Meded, A. Vijayaraghavan, L. Song, P. M. Ajayan, K. Fink, W. Wenzel and R. Krupke, *Nat. Commun.*, 2012, **4**, 1379.
32. J. Kim, S. S. Baik, S. H. Ryu, Y. Sohn, S. Park, B. G. Park, J. Denlinger, Y. Yi, H. J. Choi and K. S. Kim, *Science*, 2015, **349**, 723-726.
33. J. Sun, M. Muruganathan and H. Mizuta, *Sci. Adv.*, 2016, **2**, e1501518.
34. H. H. Pu, S. H. Rhim, M. Gajdardziksa-Josifovska, C. J. Hirschmugl, M. Weinert and J. H. Chen, *RSC Adv.*, 2014, **4**, 47481-47487.
35. H. Shi, H. Pan, Y.-W. Zhang and B. I. Yakobson, *Phys. Rev. B*, 2013, **87**, 155304.
36. T. Vy, R. Soklaski, Y. Liang and L. Yang, *Phys. Rev. B*, 2014, **89**, 235319.
37. K. H. Chen, G. H. Lu, J. B. Chang, S. Mao, K. H. Yu, S. M. Cui and J. H. Chen, *Anal. Chem.*, 2012, **84**, 4057-4062.
38. G. H. Zhou, J. B. Chang, S. M. Cui, H. H. Pu, Z. H. Wen and J. H. Chen, *ACS Appl. Mater. Interfaces*, 2014, **6**, 19235-19241.
39. G. Zhou, J. Chang, H. Pu, K. Shi, S. Mao, X. Sui, S. Cui and J. Chen, *ACS Sens.*, 2015, **1**, 295-302.
40. K. S. Novoselov, A. K. Geim, S. V. Morozov, D. Jiang, Y. Zhang, S. V. Dubonos, I. V. Grigorieva and A. A. Firsov, *Science*, 2004, **306**, 666-669.
41. F. Schwierz, *Nat. Nanotechnol.*, 2010, **5**, 487-496.
42. Tawfik A. Saleh, Mutasem M. Al-Shalalfeh and A. A. Al-Saadi, *Sci. Rep.*, 2016, **6**, 32185.
43. Tawfik A. Saleh, Mutasem M. Al-Shalalfeh and A. A. Al-Saadi, *Mater. Res. Bull.*, 2017, **91**, 173 -178.
44. S. B. Darling, *J. Appl. Phys.*, 2018, **124**, 030901.
45. L. Pauling, *The Chemical Bond*, Cornell University Press, Ithaca, New York, 1967.
46. J. A. Dean, *Lange's Handbook of Chemistry*, McGraw-Hill, 15 edn., 1999.
47. P. Giannozzi, S. Baroni, N. Bonini, M. Calandra, R. Car, C. Cavazzoni, D. Ceresoli, G. L. Chiarotti, M. Cococcioni, I. Dabo, A. Dal Corso, S. de Gironcoli, S. Fabris, G. Fratesi, R. Gebauer, U. Gerstmann, C. Gougoussis, A. Kokalj, M. Lazzeri, L. Martin-Samos, N. Marzari, F. Mauri, R. Mazzarello, S. Paolini, A. Pasquarello, L. Paulatto, C. Sbraccia, S. Scandolo, G. Sclauzero, A. P. Seitsonen, A. Smogunov, P. Umari and R. M. Wentzcovitch, *J. Phys. Condens. Matter*, 2009, **21**, 395502.
48. J. P. Perdew, K. Burke and M. Ernzerhof, *Phys. Rev. Lett.*, 1996, **77**, 3865-3868.
49. R. Hultgren, Gingrich, N. S. & Warren, B. E. , *J. Chem. Phys.*, 1935, **3**, 351–355.
50. S. Grimme, *J. Comput. Chem.*, 2006, **27**, 1787-1799.

51. B. Hans-Jurgen, K. Graf and M. Kappl, *Physics and chemistry of interfaces*, Wiley-VCH, Germany, 2006.
52. L. K. Li, Y. J. Yu, G. J. Ye, Q. Q. Ge, X. D. Ou, H. Wu, D. L. Feng, X. H. Chen and Y. B. Zhang, *Nat. Nanotechnol.*, 2014, **9**, 372-377.
53. A. L. Myers and J. M. Prausnitz, *A.I.Ch.E. Journal*, 1965, **11**, 121-127.
54. N. Gao, W. Zhou, X. Jiang, G. Hong, T.-M. Fu and C. M. Lieber, *Nano Lett.*, 2015, **15**, 2143-2148.
55. G. S. Kulkarni and Z. Zhong, *Nano Lett.*, 2012, **12**, 719-723.
56. E. Stern, R. Wagner, F. J. Sigworth, R. Breaker, T. M. Fahmy and M. A. Reed, *Nano Lett.*, 2007, **7**, 3405-3409.
57. D. Karunasagar, J. Arunachalam and S. Gangadharan, *J. Anal. At. Spectrom.*, 1998, **13**, 679-682.
58. G. H. Chen, W. Y. Chen, Y. C. Yen, C. W. Wang, H. T. Chang and C. F. Chen, *Anal. Chem.*, 2014, **86**, 6843-6849.
59. Y. Zhang, H. Zhao, Z. J. Wu, Y. Xue, X. F. Zhang, Y. J. He, X. J. Li and Z. B. Yuan, *Biosens. Bioelectron.*, 2013, **48**, 180-187.
60. K. L. Kuntz, R. Wells, T. Yang, B. Dong, J. Wang, Z. Zhang, J. Guan, D. Tomanek and S. Warren, *MRS fall meeting*, 2015.
61. J. Kang, J. D. Wood, S. A. Wells, J.-H. Lee, X. Liu, K.-S. Chen and M. C. Hersam, *Acs Nano*, 2015, **9**, 3596-3604.
62. J. D. Wood, S. A. Wells, D. Jariwala, K.-S. Chen, E. Cho, V. K. Sangwan, X. Liu, L. J. Lauhon, T. J. Marks and M. C. Hersam, *Nano Lett.*, 2014, **14**, 6964-6970.
63. J. Kang, S. A. Wells, J. D. Wood, J.-H. Lee, X. Liu, C. R. Ryder, J. Zhu, J. R. Guest, C. A. Husko and M. C. Hersam, *Proc. Nat. Acad. Sci. USA*, 2016, 1602215113.
64. M. T. Edmonds, A. Tadich, A. Carvalho, A. Ziletti, K. M. O'Donnell, S. P. Koenig, D. F. Coker, B. Oezyilmaz, A. H. Castro Neto and M. S. Fuhrer, *ACS Appl. Mater. Interfaces*, 2015, **7**, 14557-14562.
65. A. Ziletti, A. Carvalho, P. E. Trevisanutto, D. K. Campbell, D. F. Coker and A. H. C. Neto, *Phys. Rev. B*, 2015, **91**, 085407.
66. P. Li, D. Zhang, J. Liu, H. Chang, Y. e. Sun and N. Yin, *ACS Appl. Mater. Interfaces*, 2015, **7**, 24396-24402.
67. C. R. Ryder, J. D. Wood, S. A. Wells, Y. Yang, D. Jariwala, T. J. Marks, G. C. Schatz and M. C. Hersam, *Nat. Chem.*, 2016, **8**, 598-603.

TOC Entry

A statistical thermodynamics model was developed to illuminate sensing mechanisms and guide design of field-effect transistor sensors using 2D nanomaterials.